2LiBH4−MgH2 in a Resorcinol−Furfural Carbon Aerogel Scaffold for Reversible Hydrogen Storage

ARTICLE *in* THE JOURNAL OF PHYSICAL CHEMISTRY C · JANUARY 2012

Impact Factor: 4.77 · DOI: 10.1021/jp2088127

11 AUTHORS, INCLUDING:

Ivan Saldan
Swedish University of Agricultural Sciences…
36 PUBLICATIONS **166** CITATIONS
SEE PROFILE

Claudio Pistidda
Helmholtz-Zentrum Geesthacht
56 PUBLICATIONS **506** CITATIONS
SEE PROFILE

Fahim Karimi
Helmholtz-Zentrum Geesthacht
17 PUBLICATIONS **100** CITATIONS
SEE PROFILE

M. Dornheim
Helmholtz-Zentrum Geesthacht
139 PUBLICATIONS **2,750** CITATIONS
SEE PROFILE

Available online at www.sciencedirect.com

SciVerse ScienceDirect

journal homepage: www.elsevier.com/locate/he

Nanoconfined $2LiBH_4$–MgH_2 for reversible hydrogen storages: Reaction mechanisms, kinetics and thermodynamics

Rapee Gosalawit-Utke [a,b,*], *Chiara Milanese* [c], *Thomas K. Nielsen* [d], *Fahim Karimi* [a], *Ivan Saldan* [a], *Klaus Pranzas* [a], *Torben R. Jensen* [d], *Amedeo Marini* [c], *Thomas Klassen* [a], *Martin Dornheim* [a]

[a] *Institute of Materials Research, Materials Technology, Helmholtz–Zentrum Geesthacht, Geesthacht 21502, Germany*
[b] *School of Chemistry, Institute of Science, Suranaree University of Technology, Nakhon Ratchasima 30000, Thailand*
[c] *Pavia Hydrogen Lab, C.S.G.I., Department of Chemistry, Physical Chemistry Division, University of Pavia, Pavia 27100, Italy*
[d] *Center for Energy Materials, iNANO and Department of Chemistry, University of Aarhus, Aarhus C8000, Denmark*

ARTICLE INFO

Article history:
Received 23 August 2012
Received in revised form
18 October 2012
Accepted 11 November 2012
Available online 21 December 2012

Keywords:
Nanoconfinement
Lithiumborohydride
Magnesium hydride
Thermodynamics
Kinetics
Reaction mechanisms

ABSTRACT

Samples of nanoconfined Reactive Hydride Composites in resorcinol–formaldehyde aerogel scaffolds (RF–CAS) are prepared by (i) direct melt infiltration of bulk $2LiBH_4$–MgH_2; and (ii) MgH_2 impregnation and $LiBH_4$ melt infiltration. The reaction mechanisms, kinetics and thermodynamics of the systems are concluded. Activation energy (E_A) and dehydrogenation enthalpies of $LiBH_4$ and MgH_2 ($\Delta H_{des,\ MgH_2} + \Delta H_{des,\ LiBH_4}$) of nanoconfined $2LiBH_4$–MgH_2 are in this work of interest. The hydrogen sorption reactions in both nanoconfined samples are reversible as shown by the recovering of $LiBH_4$ and MgH_2 after rehydrogenation. The titration results show the remarkable improvement in desorption kinetics of nanoconfined samples over the bulk material, such as more than 90% of overall hydrogen storage capacity is obtained within 2 h from the nanoconfined samples during the 1st dehydrogenation, while that of bulk material needs more than 16 h. The activation energy of the composites decreases by 27–170 kJ/mol (ΔE_A) due to nanoconfinement. For thermodynamics, ($\Delta H_{des,\ MgH_2} + \Delta H_{des,\ LiBH_4}$) calculated from DSC results of the nanoconfined samples are in the range of 41–46 kJ/mol H_2.

1. Introduction

According to the U.S. Department of Energy (DOE) targets, the system gravimetric and volumetric capacities of 9 wt.% H_2 and 81 kg H_2/m^3, respectively, together with an operating temperature below 100 °C are required for hydrogen storages in automotive applications by 2015 [1]. Complex hydrides based on ionic combination of an aluminum hydride (AlH_4^-) or borohydride (BH_4^-) anion with a cation of alkaline or alkaline earth metal (e.g., Li^+, Na^+ and Mg^{2+}) have played an important role as a promising future hydrogen storage material because of their high theoretical hydrogen storage capacities, such as 18.5 and 7.5 wt.% H_2 are achieved from $LiBH_4$ and $NaAlH_4$, respectively [2,3]. However, strong chemical bonds in these complex hydrides result in considerably higher decomposition temperatures than those mentioned by DOE. For instance, $LiBH_4$ decomposes firstly into LiH and B at a temperature above 400 °C, corresponding to a hydrogen release of 13.5 wt.% H_2, and LiH further dehydrogenates to produce Li and H at temperatures higher than 600 °C [4,5]. In

* *Corresponding author*. Tel.: +66 44 22 4654.
E-mail address: rapee.g@sut.ac.th (R. Gosalawit-Utke).
0360-3199/$ – see front matter
http://dx.doi.org/10.1016/j.ijhydene.2012.11.064

addition, rehydrogenation of LiH and B to form $LiBH_4$ requires severe conditions of 600 °C and 350 bar H_2 [6]. The Reactive Hydride Composites (RHCs) consisting of at least two thermally stable hydrides are especially attractive for solid state hydrogen storages due to their high storage capacities and thermodynamic improvement [7,8]. During dehydrogenation, the components of these two or more hydrides react with each other, resulting in the reduction of dehydrogenation enthalpy and temperature [9,10]. For example, a well-known investigated RHC of $2LiBH_4$–MgH_2 revealed the reduction in de/rehydrogenation enthalpy by 25 kJ/mol H_2 with respect to pristine $LiBH_4$ upon MgB_2 formation during dehydrogenation [7,11]. Nevertheless, the practical application of $2LiBH_4$–MgH_2 composite is hampered by the grain growth and phase separation during hydrogen release and uptake cycles [12].

Nanoengineering based on a confinement of metal hydrides (e.g., MgH_2), complex hydrides (e.g., $LiBH_4$) and composite hydrides (e.g., $2LiBH_4$–MgH_2) in an inert nanoporous scaffold is currently considered as a promising approach to enhance sorption kinetics and thereby to lower reaction temperatures. The nanoporous scaffold material serves not only as a nanoscale structure-directing agent, but also as a host medium, prohibiting particle growth and phase separation during cycling. Therefore, nanoconfinement ensures shorter diffusion distances for hydrogen and other light elements within the nanoscale structure, yielding faster hydrogen desorption and absorption rates [13,14]. Magnesium hydride was found to be nanoconfined into the carbon aerogel scaffold via (i) melt infiltration of metallic Mg, followed by hydrogenation to MgH_2 [15,16]; and (ii) hydrogenation of nanoconfined dibutylmagnesium ($MgBu_2$) precursor to produce MgH_2 [17,18]. In the case of complex hydrides, nanoconfinement of $LiBH_4$ in the carbon aerogel scaffolds was prepared by either melt infiltration or solution impregnation [19,20]. Furthermore, to improve the hydrogen storage capacity and kinetics of the system, nanoconfinement of the composite $2LiBH_4$–MgH_2 was considered. Nielsen et al. nanoencapsulated $LiBH_4$ and MgH_2 in resorcinol–formaldehyde (RF) carbon aerogel scaffold via MgH_2 impregnation using $MgBu_2$ precursor and melt infiltration of $LiBH_4$ [14]. Moreover, direct melt infiltration of bulk $2LiBH_4$–MgH_2 composites in the RF carbon aerogel scaffold was carried out with respect to the assumption that molten $LiBH_4$ played an important role to infiltrate nanoparticle MgH_2 into the nanopores of carbon aerogel scaffold [21]. It was found that kinetic properties of the nanoconfined metal hydrides, complex hydrides or composite hydrides were significantly improved with the pore size of the scaffold-smaller pores encourage faster desorption rates. Besides, not only kinetics is affected by nanoscale influences, but thermodynamics is also theoretically predicted to differ from the bulk counterparts for small nanopores in the range of a few nm or less. Wagemans et al. reported a first-principle calculation, implying the substantial reduction in dehydrogenation enthalpy for nanoparticle MgH_2 (~1.3 nm) with respect to the bulk sample [22].

In the present work, we focus on two different systems of the nanoconfined $2LiBH_4$–MgH_2 in resorcinol–formaldehyde carbon aerogel scaffold (RF–CAS) prepared by (i) direct melt infiltration of bulk $2LiBH_4$–MgH_2; and (ii) impregnation of MgH_2 (via $MgBu_2$ precursor) and melt infiltration of $LiBH_4$. The reaction mechanisms and desorption kinetics are revealed. Moreover, further studies on kinetics (activation energy, E_A) and thermodynamics (dehydrogenation enthalpies, ΔH) are presented. Concurrently, bulk $2LiBH_4$–MgH_2 is also investigated by the similar experiments with the nanoconfined $2LiBH_4$–MgH_2 samples for comparison.

2. Experimental details

2.1. Sample preparation

2.1.1. Bulk $2LiBH_4$–MgH_2

The powder samples of 3.12 g $LiBH_4$ (90+% hydrogen storage grade, Aldrich) and 1.88 g MgH_2 (hydrogen storage grade, Aldrich) were milled in a 2:1 mol ratio using a Fritsch Pulverisette 6 classic line planetary mill under an argon atmosphere in a glove box. The mixture was milled in a stainless steel vial (Evico Magnetic, Germany) with a ball-to-powder weight ratio (BPR) of 10:1. Milling was performed for 5 h at 400 rpm.

2.1.2. Resorcinol–formaldehyde carbon aerogel scaffold (RF–CAS)

The resorcinol–formaldehyde (RF) aerogel was synthesized according to previously published procedures [23,24]. The mixture of 10.3513 g resorcinol (99%, Aldrich), 14.20 mL a 37 wt.% formaldehyde in water stabilized by methanol (Merck), 14.30 mL deionized water, and 0.0397 g Na_2CO_3 (99.999%, Aldrich) was continuously stirred in a beaker until homogeneity. The solution was poured into a polystylene bottle (50 mL) and sealed with a lid. The mixtures were initially aged at room temperature (24 h), 50 °C (24 h) and 90 °C (72 h), and left in air to cool naturally. Monoliths of blackish solid gel were infiltrated in excess amounts of acetone. The acetone bath was displaced twice within a period of 34 h. The gels were left to dry in a fume hood for several days. The monolithic gels were cut into smaller pieces (ca. 0.4 cm^3) and pyrolyzed in a tube oven under a nitrogen flow, at 800 °C (heating rate of 2.6 °C/min) and dwelling for 6 h at 800 °C. The furnace was switched off, and the samples were cooled in to room temperature. The obtained gels were treated by drying at 500 °C under vacuum for 16 h to obtain RF carbon aerogel scaffold, denoted as RF–CAS.

2.1.3. Nanoconfined $2LiBH_4$–MgH_2 in RF–CAS via direct melt infiltration

The mixture of RF–CAS and bulk $2LiBH_4$–MgH_2 at a weight ratio of 2:1 was ground in mortar. This procedure was performed under a purified argon atmosphere in a glove box. Nanoconfined $2LiBH_4$–MgH_2 was carried out using a carefully Sievert-type apparatus (a PCTPro-2000 from Hy-Energy LLC) via direct melt infiltration. The powder sample was heated to 310 °C (5 °C/min) under hydrogen pressure of 60 bar, dwelled at 310 °C for 30 min, and cooled to room temperature, denoted as nanoconfined $2LiBH_4$–MgH_2–RF.

2.1.4. Nanoconfined $2LiBH_4$–MgH_2 in RF–CAS via MgH_2 impregnation and $LiBH_4$ melt infiltration

Monoliths of RF–CAS (0.7558 g) were covered with excess amounts of a solution consisting 1 M dibutylmagnesium

($MgBu_2$) in heptane (Aldrich). This procedure was performed under a purified argon atmosphere in the glove box. The aerogel was left to dry for several days. As heptane was evaporated, $MgBu_2$ was crystallized in the pores. The white crystalline $MgBu_2$ deposited on RF–CAS surface was carefully removed mechanically. Hydrogenation of $MgBu_2$ infiltrated in RF–CAS was carried out using a carefully Sievert-type apparatus (a PCTPro-2000 from Hy-Energy LLC) at 170 °C under a hydrogen pressure of 50 bar to produce MgH_2. The sample of MgH_2–RF–CAS (1.57 g) was mixed with 0.2564 g $LiBH_4$ (>90%, Aldrich). Subsequently, $LiBH_4$ was nanoconfined into the MgH_2–RF aerogel by melt infiltration at 300 °C and $p(H_2)$ = 50 bar, denoted as nanoconfined $2LiBH_4$–$MgBu_2$–MgH_2–RF. The uptake of MgH_2 and $LiBH_4$ in RF–CAS was calculated by measuring the weight differences of the RF aerogel before and after loading with MgH_2 and $LiBH_4$.

2.2. Characterizations

The nanoporous RF–CAS was characterized by N_2 adsorption–desorption method using a Nova 2200e surface area and pore size analyzer from Quantachrome. The RF–CAS was degassed at 200 °C under vacuum for several hours, prior to the measurements. A full adsorption and desorption isotherm was measured in the pressure range of 0–1 p/p0 at liquid nitrogen temperatures with nitrogen gas as the adsorbent. Data were analyzed using the t–plot method [25,26], the Brunner Emmet Teller (BET) method [27], and the Barrett Joyner Halenda (BJH) method, and the total volume was calculated from a single point at p/p0 ~ 1 [28].

Small-angle X-ray scattering (SAXS) measurements were performed at the HASYLAB Synchrotron, at beamline BW4 in the research laboratory of DESY, Hamburg, Germany. Data was recorded with a sample-to-detector distance of 1.042 and 13.40 m using an X-ray wavelength of 1.381 Å. Each scattering pattern was detected by an MAR165 CCD detector (2048 × 2048 pixels, pixel size 79.1 μm × 79.1 μm). The powder samples were mounted tightly between thin Kapton films inside the sample holder in the glove box. The raw data was evaluated by the fit2d and gnom45 programs [29].

In situ synchrotron radiation powder X-ray diffraction (SR-PXD) experiments were carried out at the MAX II Synchrotron, beamline I711 in the research laboratory MAX-lab, Lund, Sweden [30]. For each powder diffraction pattern, it was detected by a MAR165 CCD detector with selected X-ray wavelengths of 0.94608 and 1.072 Å. The powder samples were refilled airtight in sapphire capillaries under a purified argon atmosphere in the glove box. The powder samples of both nanoconfined $2LiBH_4$–MgH_2–RF and $2LiBH_4$–$MgBu_2$–MgH_2–RF in the states of before and after infiltration, after dehydrogenation, and after rehydrogenation were investigated by performing a single scan of the powder samples. For nanoconfined $2LiBH_4$–MgH_2–RF, the powder sample was heated from room temperature to 450 °C (10 °C/min) with various hydrogen pressures in the range of 3–150 bar. In the case of nanoconfined $2LiBH_4$–$MgBu_2$–MgH_2–RF, the powder sample was heated from room temperature to 450 °C with the heating rates from 10 to 15 °C/min, and the hydrogen pressure was from 6 to 150 bar. The program used to evaluate SR–PXD data was fit2d [21].

Dehydrogenation, rehydrogenation and cycle efficiency were studied with a carefully calibrated Sievert-type apparatus (a PCTPro-2000 from Hy-Energy LLC). The powder samples (~120 mg) were filled in a high pressure–temperature vessel and transferred to Sievert-type apparatus. Dehydrogenations of both nanoconfined $2LiBH_4$–MgH_2–RF and $2LiBH_4$–$MgBu_2$–MgH_2–RF were carried out at 425 °C (5 °C/min) under 3.4 bar H_2. For rehydrogenation, the dehydrogenated powders were heated to 425 °C (5 °C/min) under the hydrogen pressure of ~130–145 bar and dwelled at 425 °C for 10–12 h. For comparison, bulk $2LiBH_4$–MgH_2 was also dehydrogenated and rehydrogenated by similar procedures.

Coupled manometric–calorimetric measurements of bulk $2LiBH_4$–MgH_2, and nanoconfined $2LiBH_4$–MgH_2–RF and $2LiBH_4$–$MgBu_2$–MgH_2–RF were carried out by connecting a manometric apparatus (a PCTPro-2000, Setaram&Hy-Energy) with a high-pressure calorimeter (a Sensys DSC, Setaram). A high-pressure cell of the calorimeter, connected to the manometric instrument by a 1/8 in. stainless steel tube, was loaded with about 13–25 mg of the powder samples in the glove box. Dehydrogenations were performed by heating the samples from room temperature up to 480 °C for both nanoconfined samples and to 560 °C for bulk material with the heating rates of 2, 5, 10 and 15 °C/min under hydrogen pressure of 3 bar. In order to evaluate the melting enthalpy of $LiBH_4$, nanoconfined $2LiBH_4$–MgH_2–RF and $2LiBH_4$–$MgBu_2$–MgH_2–RF were heated up to 400 °C (5 °C/min) under 100 bar H_2. Dehydrogenation enthalpies were achieved by heating the samples (5 °C/min) up to 560 and 480 °C for bulk and nanoconfined samples, respectively. Peak area under each dehydrogenation step was taken into account for dehydrogenation enthalpy calculation. The calorimetric profiles were elaborated by a Calisto software to obtain the enthalpy results and peak temperatures [31].

3. Results and discussion

3.1. Nanoconfinement and reaction mechanisms

Chemically inert RF–CAS with a surface area (S_{BET}) of 682 m^2/g and an average pore size (D_{max}) of 31 nm (Table S1 in supplementary material) was used as a nanoporous scaffold material in this study. In the previous studies, nanoconfinement of the composite hydride ($2LiBH_4$–MgH_2) in RF–CAS was clearly clarified by several means, such as *in situ* synchrotron radiation powder X-ray diffraction (SR–PXD), scanning electron microscopy-energy dispersive X-ray spectroscopy (SEM–EDS) and continuous DSC–TG–MS [13,14]. For the present work, small angle X–ray scattering (SAXS) was additionally performed to evaluate the confinement of the composite hydride in RF–CAS. Fig. 1 reveals the highest pore size distribution of the RF–CAS at about 38 nm, slightly larger than the pristine RF–CAS (31 nm pore size) shown in Table S1. After infiltration with the composite hydride $2LiBH_4$–MgH_2, both nanoconfined samples reveal the decrease of pore volume in RF–CAS, suggesting successful nanoconfinement. Not only the information based on successful nanoconfinement, already confirmed by other means in the previous studies, is obtained from SAXS results, but also it is found that

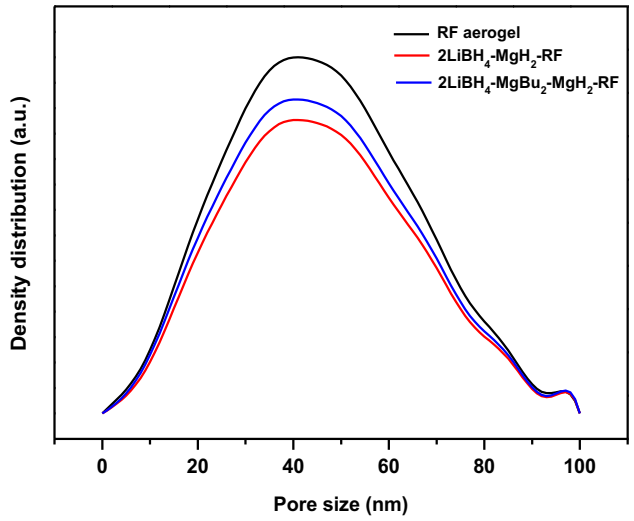

Fig. 1 – Size distribution function of RF–CAS, nanoconfined $2LiBH_4$–MgH_2–RF and $2LiBH_4$–$MgBu_2$–MgH_2–RF samples.

the pore volume after infiltration is not significantly decreased. This implies that there are still vacancies in the nanoporous structure of RF–CAS for more hydride composite confinement.

The reaction mechanisms during infiltration, dehydrogenation and rehydrogention of both nanoconfined $2LiBH_4$–MgH_2–RF and $2LiBH_4$–$MgBu_2$–MgH_2–RF were identified by *in situ* synchrotron radiation powder X-ray diffraction (SR–PXD). Fig. 2(A)(a) shows the diffraction peaks of *o*–$LiBH_4$ and MgH_2 of the bulk $2LiBH_4$–MgH_2. After melt infiltration performed by heating the mixture of bulk $2LiBH_4$–MgH_2 and RF–CAS to 350 °C (10 °C/min) under 60 bar H_2, dwelling at 350 °C for 30 min, and cooling to room temperature, the single scan shows the disappearance of the $LiBH_4$ diffraction peaks, referring to amorphous and/or nanosized $LiBH_4$ as it was obtained from complete melt infiltration in RF–CAS (Fig. 2(A)(b)). Moreover, the diffraction peaks of MgH_2, Mg, MgB_2, and MgO as well as a broad region in the 2θ range of 10–15°, corresponding to the graphite-like structure within the RF–CAS are detected [32]. The formation of MgB_2 suggests the partial dehydrogenation of both MgH_2 and $LiBH_4$ during melt infiltration. Continuously, dehydrogenation was proceeded on infiltrated sample by heating the sample to 450 °C (10 °C/min) under 3–6 bar H_2, dwelling at 450 °C for 30 min, and cooling to room temperature. From Fig. 2(A)(c), the similar diffraction peaks as in the infiltration profile; that is, Mg, MgB_2, and MgO are observed in accordance with the dehydrogenation of bulk $2LiBH_4$–MgH_2 [7]. Afterward, rehydrogenation was carried out by heating the dehydrogenated sample to 450 °C (10 °C/min) under 130 bar H_2, keeping at 450 °C for 1 h, and cooling to room temperature. Fig. 2(A)(d) exhibits the diffraction peaks of $LiBH_4$, MgH_2, MgO and unknown phase. The presences of $LiBH_4$ and MgH_2 after rehydrogenation imply the reversibility of the nanoconfined $2LiBH_4$–MgH_2–RF, which is a very important requirement for hydrogen storage applications. For the nanoconfined $2LiBH_4$–$MgBu_2$–MgH_2–RF, the diffraction peaks of $MgBu_2$ and *o*–$LiBH_4$ together with the broad region (2θ = 10–15°) corresponding to the graphite–like structure of

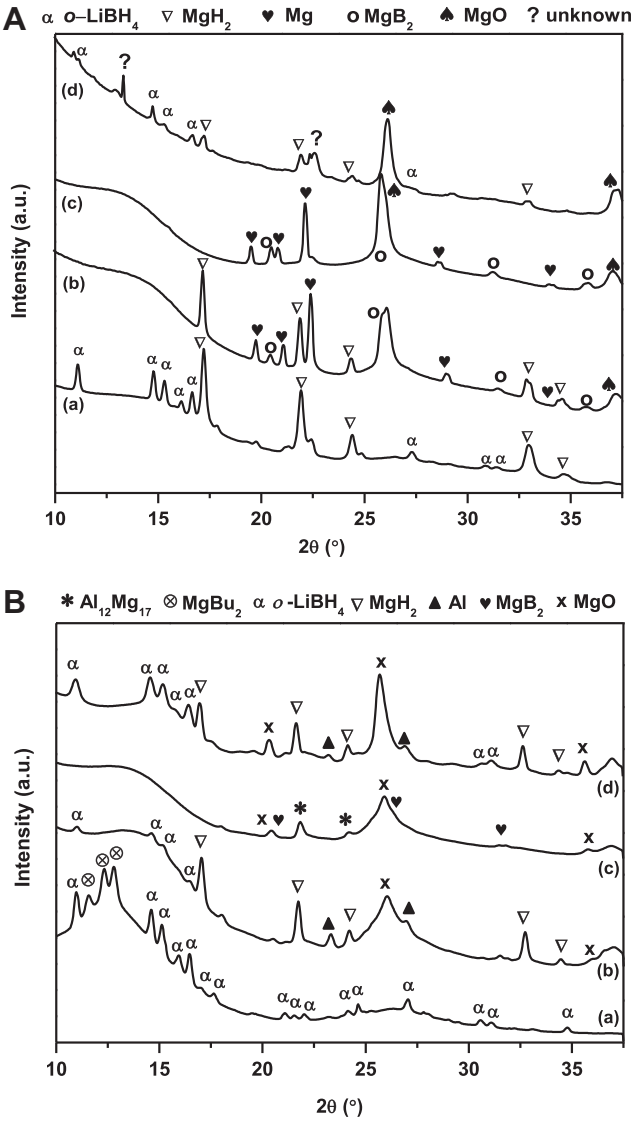

Fig. 2 – SR–PXD single scans of the nanoconfined $2LiBH_4$–MgH_2–RF (λ = 0.94608 A) (A) and nanoconfined $2LiBH_4$–$MgBu_2$–MgH_2–RF (λ = 1.072 A) (B); before melt infiltration (a), after melt infiltration (b), after dehydrogenation (c), and after rehydrogenation (d).

RF–CAS are observed before infiltration (Fig. 2(B)(a)). After infiltration of $LiBH_4$ and MgH_2 in RF–CAS by heating the sample to 320 °C (10 °C/min) under hydrogen pressure of 50 bar, dwelling at 330 °C for 15 min, and cooling to room temperature, the single scan reveals the diffraction peaks of MgH_2, MgO and $LiBH_4$ (Fig. 2(B)(b)). The indications of MgH_2 and broader $LiBH_4$ peaks imply the conversion of $MgBu_2$ to MgH_2 and nanoconfinement of $LiBH_4$. Moreover, an exposure of aluminum (Al) after melt infiltration could be explained by the reduction of triethylaluminium present in the use of $MgBu_2$ solution [14]. Thereafter, the infiltrated sample was dehydrogenated by heating the sample to 450 °C (10 °C/min) under hydrogen pressure of 3–6 bar and cooling to room temperature. Fig. 2(B)(c) shows the diffraction peaks of MgO as

well as MgB_2 and a new phase of $Al_{12}Mg_{17}$. After rehydrogenation by heating the dehydrogenated sample to 450 °C (15 °C/min) under hydrogen pressure of 150 bar, dwelling at 450 °C for 1 h and 13 min, and cooling to room temperature, the diffraction peaks of $LiBH_4$ and MgH_2 are recovered as well as those of MgO (Fig. 2(B)(d)). This suggests the reversibility of the nanoconfined $2LiBH_4$–$MgBu_2$–MgH_2–RF hydrogen storage system. Furthermore, it is important to note that, no indication of any chemical reaction between RF–CAS and composite hydrides was found. As shown in Fig. 2(B)(c), an appearance of Al causes the unrequired reaction with Mg to form $Al_{12}Mg_{17}$ during dehydrogenation step. In addition, it's well known that Al thermodynamically destabilize Mg [33]. Therefore, to avoid this mistake in the next investigations of kinetics (activation energy) and thermodynamics (dehydrogenation enthalpy), a new sample of nanoconfined $2LiBH_4$–$MgBu_2$–MgH_2–RF without Al is further studied.

3.2. *Dehydrogenation kinetics (titration measurements)*

To evaluate the dehydrogenation kinetics, four hydrogen release and uptake cycles of both nanoconfined $2LiBH_4$–MgH_2–RF and $2LiBH_4$–$MgBu_2$–MgH_2–RF as well as two cycles of the bulk $2LiBH_4$–MgH_2 were carried out by titration measurements. In order to properly compare the kinetics of the samples, normalized dehydrogenation profiles are considered. Normalization is carried out by using the highest wt.% H_2 released from each cycle, corresponding to complete dehydrogenation, as a reference value. Each normalized curve refers to the ratio between H_2 wt.% during dehydrogenation and that at complete dehydrogenation. Thus, normalization profile suggests how fast hydrogen desorption can be achieved. Fig. 3 shows that both nanoconfined $2LiBH_4$–MgH_2–RF and $2LiBH_4$–$MgBu_2$–MgH_2–RF release more than 90% of total hydrogen storage capacities after 2 h during the 1st cycle. In the case of the 2nd, 3rd and 4th cycles, both nanoconfined samples reveal comparable desorption kinetics with 90% of total dehydrogenation capacities reached after 4–8 h. With respect to the 1st and 2nd desorptions, nanoconfined samples give remarkably superior

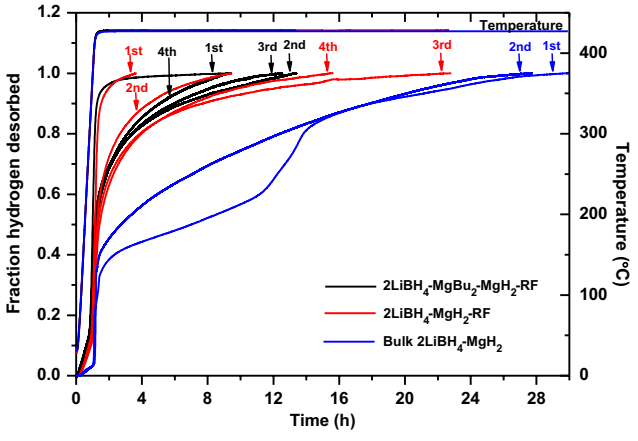

Fig. 3 – Normalized hydrogen desorption profiles of bulk $2LiBH_4$–MgH_2, and nanoconfined $2LiBH_4$–MgH_2–RF and $2LiBH_4$–$MgBu_2$–MgH_2–RF.

desorption kinetics than the bulk $2LiBH_4$–MgH_2. For example, more than 26 h is required for total dehydrogenation of bulk material during the 1st and 2nd cycles, whereas those of nanoconfined samples need not more than 12 h. This suggests significant improvement of kinetics in both nanoconfined samples as compared to the bulk material.

3.3. *Dehydrogenation profiles and capacities*

In general, to prove that the experimental data is reliable, comparison with the theoretical values is required. The theoretical hydrogen storage capacities of each sample calculated from the amount of all components in the mixtures are shown in Table 1. Bulk $2LiBH_4$–MgH_2 contains $LiBH_4$ and MgH_2 of 62.9 and 37.1 wt.%, respectively. The amount of RF–CAS, $LiBH_4$ and MgH_2 in the nanoconfined $2LiBH_4$–MgH_2–RF are 66.7, 20. 9, and 12.4 wt.%, respectively. In the case of the nanoconfined $2LiBH_4$–$MgBu_2$–MgH_2–RF (with Al), they are 64.8, 21.9, and 13.3 wt.% for RF–CAS, $LiBH_4$ and MgH_2, respectively, while those of the one without Al are 72.7, 17.0, and 10.3, respectively. The molar ratio of $LiBH_4$:MgH_2 obtained from bulk and all nanoconfined samples is comparable as 2:1. On the basis of the bulk $2LiBH_4$–MgH_2 (2:1 mol ratio of $LiBH_4$:MgH_2), 11.43 wt.% H_2 is obtained as a theoretical storage capacity calculated from the following equation.

$$2LiBH_{4(l)} + MgH_{2(s)} \leftrightarrow 2LiH_{(s)} + MgB_{2(s)} + 4H_{2(g)} \quad (1)$$

Therefore, the theoretical hydrogen storage capacities of the nanoconfined samples of $2LiBH_4$–MgH_2– RF and $2LiBH_4$–$MgBu_2$–MgH_2–RF are 3.81, and 4.02 (with Al) and 3.11 (without Al) wt.% H_2, respectively (Table 1). The significant difference in theoretical hydrogen storage capacities of the nanoconfined $2LiBH_4$–MgH_2–$MgBu_2$–RF with and without Al are due to the fact that Al-contaminated $MgBu_2$ solution containing triethylaluminium gives an additional weight gain, resulting in overestimated MgH_2 amount. Thus, excess of $LiBH_4$ was also added to obtain the molar ratio of 2:1 ($LiBH_4$:MgH_2). Moreover, the experimental hydrogen storage capacities of 10.5 (bulk $2LiBH_4$–MgH_2), 3.6 (nanoconfined $2LiBH_4$–MgH_2–RF), 3.9 (nanoconfined $2LiBH_4$–$MgBu_2$–MgH_2–RF (with Al)), and 2.8 wt.% (nanoconfined $2LiBH_4$–$MgBu_2$–MgH_2–RF (without Al)) are reported in Table 1.

Coupled manometric–calorimetric analysis under 5 °C/min heating rate was performed to characterize the dehydrogenation profiles of bulk and nanoconfined samples. Fig. 4(A) shows the endothermic peaks of *o*-$LiBH_4$ to *h*-$LiBH_4$ phase transformation and *h*-$LiBH_4$ melting of the bulk material at 115.6 and 289.7 °C, respectively, in agreement with the previous studies [7]. By heating the sample up to 386.2 and 493.6 °C, endothermic peaks implying dehydrogenations of MgH_2 and $LiBH_4$ are observed, respectively. The manometric result reveal 10.56 wt.% H_2 released, approaching to the theoretical hydrogen storage capacity (11.43 wt.%) and that from the experiment (after 1st desorption, 10.5 wt.%) (Table 1). For comparison, the coupled manometric–calorimetric analysis was also performed on both nanocofined samples. From Fig. 4(B), the nanoconfined $2LiBH_4$–MgH_2–RF exhibits the endothermic peaks corresponding to phase transformation and melting of $LiBH_4$ at 105.2 and 269.9 °C, respectively, while

Table 1 – Amount of components, molar ratio of $LiBH_4$:MgH_2 in the RF–CAS, and theoretical and experimental hydrogen storage capacities of bulk and nanoconfined samples.

Samples	Amount of components (wt.%)			Molar ratio of $LiBH_4$:MgH_2	Theoretical H_2 storage capacities (wt.% H_2)	Experimental H_2 storage capacities after 1st desorption (wt.% H_2)
	RF–CAS	$LiBH_4$	MgH_2			
Bulk $2LiBH_4$–MgH_2	–	62.9	37.1	2:1	11.43	10.5[a]
$2LiBH_4$–MgH_2–RF	66.7	20.9	12.4	2:1	3.81	3.6[a]
$2LiBH_4$–$MgBu_2$–MgH_2–RF (with Al)	64.8	21.9	13.3	2:1	4.02	3.9[b]
$2LiBH_4$–$MgBu_2$–MgH_2–RF (without Al)	72.7	17.0	10.3	2:1	3.11	2.8[c]

a Reference number [21].
b Reference number [14].
c Dehydrogenation profiles and hydrogen storage capacities from coupled manometric–calorimetric results (Fig. 4(C)).

those of MgH_2 and $LiBH_4$ dehydrogenations are at 321.5 and 382.7 °C, respectively. It should be noted that the peak temperatures of all phenomena are significantly shifted to lower values as compared to the bulk material; that is, ΔT = 10.4, 19.8, 64.7 and 110.9 °C for phase transformation, melting of $LiBH_4$, and dehydrogenations of MgH_2 and $LiBH_4$, respectively. Besides, the storage capacity of 3.35 wt.% H_2, that is, ~88 and 93% of the theoretical and experimental (after 1st desorption (Table 1) values, respectively, is observed by the manometric analysis (Fig. 4(B)). In the case of the nanoconfined $2LiBH_4$–$MgBu_2$–MgH_2–RF, the peak temperature of $LiBH_4$ phase transformation is found at 110.8 °C. Melting of $LiBH_4$, indicated by the endothermic peaks in the range of constant manometric results (0 wt.% H_2 desorption), is in accordance with the broad and sharp peaks at 261 and 286.4 °C, respectively (Fig. 4(C)). The two different melting peaks of $LiBH_4$ could be due to the partial nanoconfinement of $LiBH_4$ in the nanopores of the RF–CAS; that is, the melting of nanoconfined $LiBH_4$ performs at low temperature of 261 °C, whereas that of the surface-occupied $LiBH_4$ still requires high temperature of 286.4 °C, approaching to that of the bulk $2LiBH_4$–MgH_2 (289.7 °C). Interestingly, the dehydrogenations of MgH_2 and $LiBH_4$ are observed to be a single endothermic peak at 354.5 °C, which takes place at a significantly lower temperature than in case of bulk material (ΔT = 31.7 and 139.1 °C as compared to MgH_2 and $LiBH_4$ decompositions, respectively). For hydrogen storage capacity, significant H_2 amount of 2.83 wt.% (~91% of theoretical H_2 storage capacity) is detected by the manometric measurement. Moreover, due to partial nanoconfinement of $LiBH_4$ in RF–CAS found in both nanoconfined samples [14,21], phase transformation peak in DSC thermogram is revealed with shoulder (Fig. 4(A) and (B)). The inferior hydrogen storage capacities of both nanoconfined samples as compared with the theoretical values (Table 1) could be due to the formation of undesirable products of MgO, $Al_{12}Mg_{17}$, and unknown phase during cycling (Fig. 2(A) and (B)).

3.4. *Activation energy* (E_A)

By performing DSC measurements under different heating rates of 2, 5, 10 and 15 °C/min, the activation energy (E_A) of MgH_2 and $LiBH_4$ dehydrogenations can be calculated by Kissinger method [34] described in supplementary material, Figs. S1 and S2. As shown in Fig. S1, the dehydrogenation of $LiBH_4$ is revealed in several steps. Therefore, to assure that the activation energies (E_A) of the same $LiBH_4$ dehydrogenation step was calculated, only clear T_p at the highest values (bulk and nanoconfined $2LiBH_4$–MgH_2–RF), representing the most difficult dehydrogenation step by high temperature requirement, from DSC thermograms were considered. The Kissinger plots; that is, $\ln(\beta/T_p^2)$ as a function of the inverse T_p, are shown in Fig. 5. The activation energies (E_A) for MgH_2 and $LiBH_4$ dehydrogenations of bulk $2LiBH_4$–MgH_2 are calculated from the slope of the plots to be in the range of 221 ± 5 and 306 ± 10 kJ/mol, respectively. In the case of nanoconfined $2LiBH_4$–MgH_2–RF, the calculated E_A of 89 ± 2 and 279 ± 5 kJ/mol for MgH_2 and $LiBH_4$ dehydrogenations, respectively, are obtained (Fig. 5). With respect to the bulk material, the E_A of MgH_2 and $LiBH_4$ dehydrogenations of the nanoconfined $2LiBH_4$–MgH_2–RF are considerably shifted to the lower values of ΔE_A = 132 and 27 kJ/mol, respectively. Furthermore, E_A of the nanoconfined $2LiBH_4$–$MgBu_2$–MgH_2–RF was also evaluated by the same procedures under the heating rates of 2, 5 and 10 °C/min. From Fig. S1 (supplementary material), dehydrogenations of both MgH_2 and $LiBH_4$ under heating rates of 5 and 10 °C/min clearly combine into a single step as shown as an endothermic peak at about 354.4 and 376 °C, respectively, while those under 2 °C/min are two peaks at 339.8 and 378 °C. However, manometric results in Fig. S2 (supplementary material) clarifies single–step dehydrogenation for $2LiBH_4$–MgH_2 at all heating rates. Thus, T_p at about 50% dehydrogenation of each heating rate, representing the same dehydrogenation phenomena, are considered for E_A calculation, that is, 339.8, 354.4, and 376 °C obtained from 2, 5 and 10 °C/min, respectively (Fig. S2). From Fig. 5, calculated E_A of $LiBH_4$–MgH_2 dehydrogenation is 135 ± 5 kJ/mol. This yields the ΔE_A = 86 and 171 kJ/mol for MgH_2 and $LiBH_4$ dehydrogenations as compared with bulk material. It should be noted that both nanoconfined samples offer remarkable reduction in E_A results as compared to the bulk material, leading to kinetic improvement of the hydrogen storages. In theory, nanoconfinement effects on dehydrogenation kinetic improvement could be due to the reduced distance for hydrogen diffusion and the increase in reaction frequency, effectively accelerating the dehydrogenation process and serving as an efficient pathway for heat transfer. All E_A values obtained from each sample as well as hydrogen released

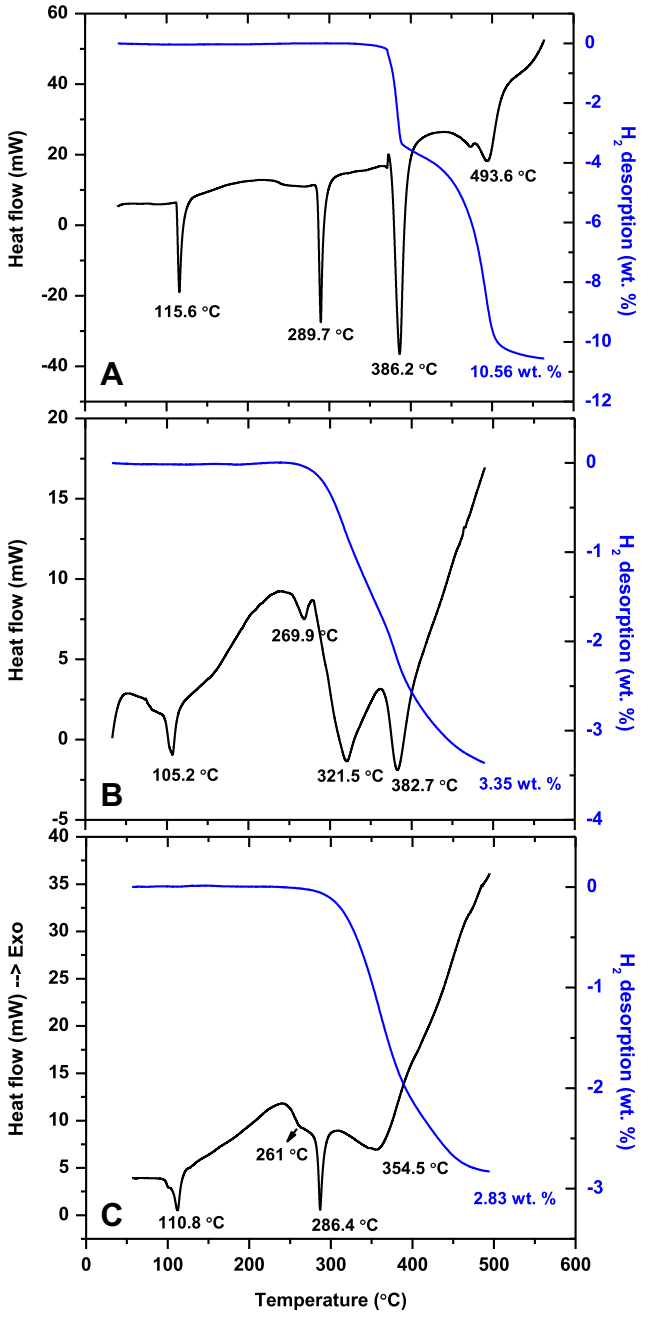

Fig. 4 – Dehydrogenation profiles and hydrogen storage capacities from coupled manometric–calorimetric analysis of bulk $2LiBH_4$–MgH_2 (A), nanoconfined $2LiBH_4$–MgH_2–RF (B), and nanoconfined $2LiBH_4$–$MgBu_2$–MgH_2–RF (C).

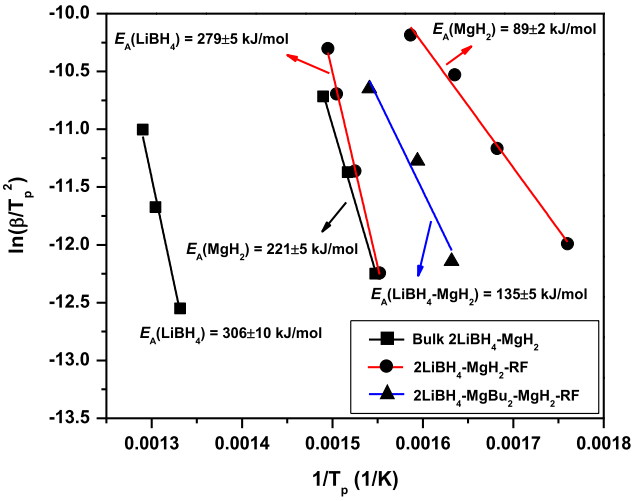

Fig. 5 – Kissinger plots representing the activation energy (E_A) of MgH_2 and $LiBH_4$ dehydrogenations of bulk and nanoconfined samples.

content with respect to hydride content are summarized in Table 2.

3.5. *Dehydrogenation enthalpies of $LiBH_4$ and MgH_2*

With respect to the literature [21] and SR–PXD results (Fig. 2) of both nanoconfined samples, the reaction mechanisms during dehydrogenation are similar to bulk $2LiBH_4$–MgH_2, where the formation of LiH and MgB_2 is achieved (Eq. (1)). The disappearance of LiH diffraction peaks in the SR–PXD patterns (Fig. 2) could be due to the fact that LiH, obtained from $LiBH_4$ dehydrogenation, is nanoconfined in the RF–CAS. On the basis of the reaction mechanisms mentioned above, the dehydrogenation enthalpies of $LiBH_4$ and MgH_2 from either bulk $2LiBH_4$–MgH_2 or nanoconfined samples can be calculated by a simple quantitative basis:

$$\begin{aligned}\Delta H_{\mathrm{rxn},\,2LiBH_4-MgH_2} &= \Sigma\Delta H_{\mathrm{products}} - \Sigma\Delta H_{\mathrm{reactants}} \\ &= \left(\Delta H_{\mathrm{form,\,LiH}} + \Delta H_{\mathrm{form,\,MgB_2}} + \Delta H_{\mathrm{form,\,H_2}}\right) \\ &\quad - \left(\Delta H_{\mathrm{des,\,MgH_2}} + \Delta H_{\mathrm{des,\,LiBH_4}}\right) \qquad (2)\end{aligned}$$

$$\begin{aligned}\left(\Delta H_{\mathrm{des,\,MgH_2}} + \Delta H_{\mathrm{des,\,LiBH_4}}\right) &= \left(\Delta H_{\mathrm{form,\,LiH}} + \Delta H_{\mathrm{form,\,MgB_2}}\right. \\ &\quad \left. + \Delta H_{\mathrm{form,\,H_2}}\right) - \Delta H_{\mathrm{rxn,\,2LiBH_4-MgH_2}} \qquad (3)\end{aligned}$$

where $\Delta H_{\mathrm{rxn,\,2LiBH_4-MgH_2}}$ is a total enthalpy of the overall dehydrogenation reaction of $2LiBH_4$–MgH_2, calculated from DSC curves, $\Delta H_{\mathrm{products}}$ and $\Delta H_{\mathrm{reactants}}$ indicate the enthalpies of products and reactants, respectively, $\Delta H_{\mathrm{form,\,LiH}}$, $\Delta H_{\mathrm{form,\,MgB_2}}$, and $\Delta H_{\mathrm{form,\,H_2}}$, are the formation enthalpies of LiH, MgB_2, and H_2, respectively, and $\left(\Delta H_{\mathrm{des,\,MgH_2}} + \Delta H_{\mathrm{des,\,LiBH_4}}\right)$ (our target) is the dehydrogenation enthalpies of MgH_2 and $LiBH_4$. Considering the reaction mechanisms of $2LiBH_4$–MgH_2 composite, the formations of MgB_2 and LiH are observed during the dehydrogenations of MgH_2 and $LiBH_4$. Therefore, the integrated area of the two endothermic peaks (at 386.2 and 493.6 °C) in DSC thermogram (Fig. 4(A)) corresponding to the total enthalpy of the overall dehydrogenation reaction of MgH_2 and $LiBH_4$ $\Delta H_{\mathrm{rxn,\,2LiBH_4-MgH_2}}$ include not only endothermic dehydrogenations of $LiBH_4$ and MgH_2, but also exothermic formations of MgB_2 and LiH. In the literature, the $\Delta H_{\mathrm{form,\,LiH}}$, $\Delta H_{\mathrm{form,\,MgB_2}}$ and $\Delta H_{\mathrm{form,\,H_2}}$ are −90.63 kJ/mol LiH, −91.06 kJ/mol MgB_2 and 0 kJ/mol H_2, respectively [35]. From Eq. (1), $LiBH_4$ reacts with MgH_2 (molar ratio of 2:1) to produce LiH, MgB_2, and H_2 (molar ratio of 2:1:4). With respect to these molar ratios of all reactants and products in Eq. (1), 2 mol of LiH, equivalent to 4 mol of H_2, require (−90.63 × 2) kJ as formation enthalpy; thus,

Table 2 – Hydrogen storage capacities, activation energy (E_A), and dehydrogenation enthalpies of MgH_2 and $LiBH_4$ ($\Delta H_{des,\ MgH_2} + \Delta H_{des,\ LiBH_4}$) of bulk and nanoconfined samples together with reference values.

Samples	H_2 desorbed (wt.%)	Activation energy (E_A) (kJ/mol)		Dehydrogenation enthalpies of $LiBH_4$ and MgH_2 ($\Delta H_{des,\ MgH_2} + \Delta H_{des,\ LiBH_4}$) (kJ/mol H_2)
		MgH_2	$LiBH_4$	
Bulk $2LiBH_4$–MgH_2	10.6[a]	221 ± 5	306 ± 10	44.13
$2LiBH_4$–MgH_2–RF	10.1[a]	89 ± 2	279 ± 5	46.21
$2LiBH_4$–$MgBu_2$–MgH_2–RF (without Al)	10.4[a]	135 ± 5[d]		41.47
Bulk $2LiBH_4$–MgH_2	11.4[b]	157[c]	–	45.8[e]

a Results from manometric measurements calculated with respect to composite hydride ($2LiBH_4$–MgH_2) content.
b Theoretically calculated value.
c Activation energy (E_A) of MgH_2 dehydrogenation obtained from the hydride composite $2LiBH_4$–MgH_2 under the weight ratio of 2:1 (Ref. [34]).
d E_A of $LiBH_4$–MgH_2 dehydrogenation.
e Dehydrogenation enthalpies of $LiBH_4$ and MgH_2 ($\Delta H_{des,\ MgH_2} + \Delta H_{des,\ LiBH_4}$) (Ref. [36]).

based on the mole of H_2 the formation enthalpy of LiH in the unit of kJ/mol H_2 can be calculated to be $(-90.63 \times 2)/4 = -45.31$ kJ/mol H_2. In the case of MgB_2, the same principle is used to estimate the formation enthalpy to be $(-91.06 \times 1)/4 = -22.77$ kJ/mol H_2. These formation enthalpies of LiH and MgB_2 refer to heat release during formation as well as the heat used to dissociate the chemical bonds in the molecules. According to Eq. (3), $\Delta H_{rxn,\ 2LiBH_4-MgH_2}$ is calculated based on the dissociation enthalpy. Here, the $\Delta H_{form,\ LiH}$ and $\Delta H_{form,\ MgB_2}$ values used for enthalpy studies are similar to the formation enthalpies but in the positive forms as 45.31 and 22.77 kJ/mol H_2, respectively. For our target ($\Delta H_{des,\ MgH_2} + \Delta H_{des,\ LiBH_4}$), it can be calculated by substituting the values of $\Delta H_{rxn,\ 2LiBH_4-MgH_2}$ (from DSC thermogram), $\Delta H_{form,\ LiH}$, and $\Delta H_{form,\ MgB_2}$ in Eq. (3). From Fig. 6, bulk $2LiBH_4$–MgH_2 shows the measured enthalpies (integrated peak area) of phase transformation, melting of $LiBH_4$, and overall dehydrogenations of MgH_2 and $LiBH_4$ ($\Delta H_{rxn,\ 2LiBH_4-MgH_2}$) as 1.51, 2.78, and 23.95 kJ/mol H_2, respectively. By using the value of $\Delta H_{rxn,\ 2LiBH_4-MgH_2}$, $\Delta H_{form,\ LiH}$, and $\Delta H_{form,\ MgB_2}$, ($\Delta H_{des,\ MgH_2} + \Delta H_{des,\ LiBH_4}$) can be calculated to be 44.13 kJ/mol H_2. This value approaches to the calculated enthalpy of $2LiBH_4$–MgH_2 system (45.8 kJ/mol H_2) reported elsewhere [36].

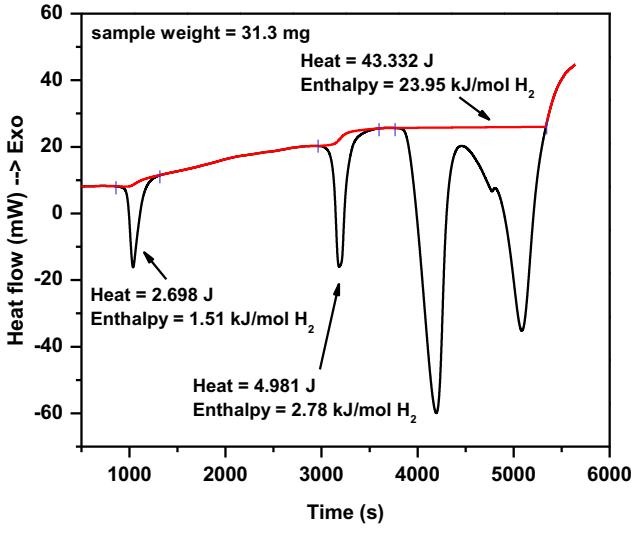

Fig. 6 – Enthalpy calculations of bulk $2LiBH_4$–MgH_2 during dehydrogenation.

Further investigation was carried out on the nanoconfined $2LiBH_4$–MgH_2–RF sample. From the coupled manometric–calorimetric analysis (Fig. 4(B)), it is found that an endothermic peak at 269.9 °C corresponding to *h*–$LiBH_4$ melting overlaps with the dehydrogenation peaks of MgH_2 and $LiBH_4$. Therefore, to obtain the accurate dehydrogenation enthalpy, the melting enthalpy of *h*–$LiBH_4$ must be previously measured. Fig. 7(A) clarifies the melting enthalpy of *h*–$LiBH_4$ obtained by heating the powder sample of nanoconfined $2LiBH_4$–MgH_2–RF up to 400 °C (5 °C/min) under the hydrogen pressure of 100 bar. The high hydrogen pressure (100 bar) applied was to protect dehydrogenation during heating. The phase transformation and melting enthalpies of $LiBH_4$ are calculated to be 0.94 and 8.76 kJ/mol H_2, respectively (Fig. 7(A)). To achieve only the overall dehydrogenation enthalpies of MgH_2 and $LiBH_4$ ($\Delta H_{rxn,\ 2LiBH_4-MgH_2}$), the calculated enthalpy of the second endothermic region in Fig. 7(B) (30.63 kJ/mol H_2), the combination of $LiBH_4$ melting and overall dehydrogenations enthalpies, is subtracted with $LiBH_4$ melting enthalpy obtained from Fig. 7(A). Therefore, the calculated $\Delta H_{rxn,\ 2LiBH_4-MgH_2}$ is $30.63-8.76 = 21.87$ kJ/mol H_2. This results in ($\Delta H_{des,\ MgH_2} + \Delta H_{des,\ LiBH_4}$) of 46.21 kJ/mol H_2 for the nanoconfined $2LiBH_4$–MgH_2–RF.

In the case of nanoconfined $2LiBH_4$–$MgBu_2$–MgH_2–RF, melting enthalpy of *h*–$LiBH_4$ was also investigated separately from the dehydrogenation experiment as in the nanoconfined $2LiBH_4$–MgH_2–RF. Fig. 8(A) reveals the phase transformation and melting enthalpies of $LiBH_4$ as 1.12 and 5.25 kJ/mol H_2, respectively. Furthermore, Fig. 8(B) shows combined enthalpies of $LiBH_4$ melting and overall MgH_2 and $LiBH_4$ dehydrogenations as 31.86 kJ/mol H_2. From Fig. 8(A) and (B); thus, the $\Delta H_{rxn,\ 2LiBH_4-MgH_2}$ is estimated to be $31.86-5.25 = 26.61$ kJ/mol H_2, yielding 41.47 kJ/mol H_2 for ($\Delta H_{des,\ MgH_2} + \Delta H_{des,\ LiBH_4}$). Thermodynamics properties based on the dehydrogenation enthalpy of $LiBH_4$ and MgH_2 ($\Delta H_{des,\ MgH_2} + \Delta H_{des,\ LiBH_4}$) obtained from DSC measurements of the bulk and nanoconfined samples are comparable in the range of 41.5–46.2 kJ/mol H_2. Due to the fact that the particle size of confined metal hydride, relevant to the pore size of RF–CAS (31 nm), is greater than the nanoconfined metal hydrides (1.3 nm) in the literature [22], where

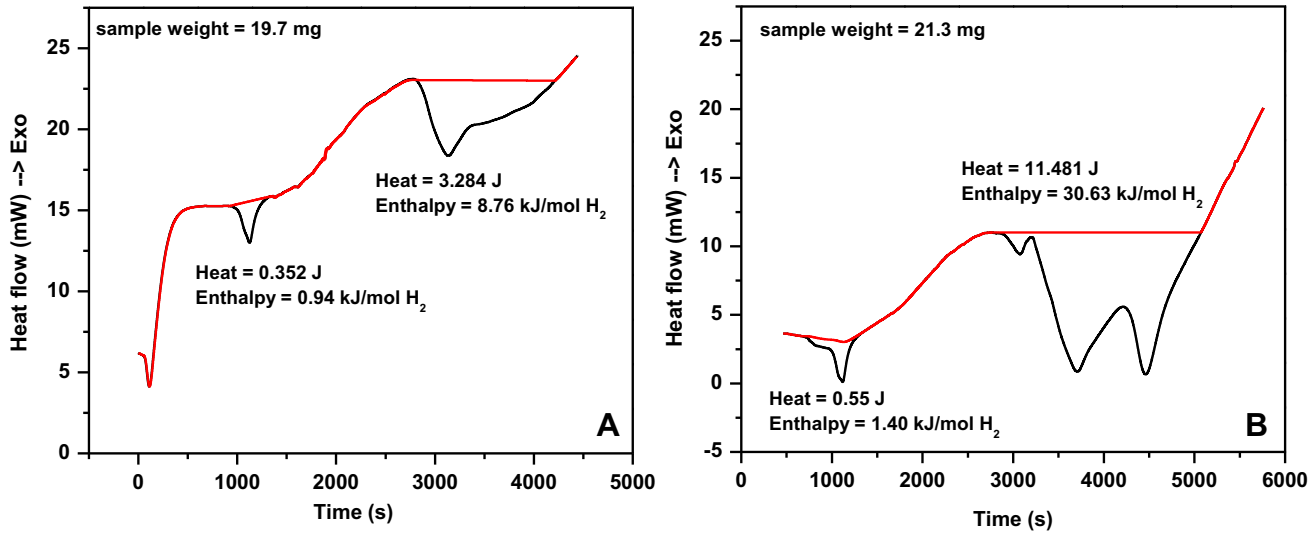

Fig. 7 – Enthalpy calculations of the nanoconfined $2LiBH_4$–MgH_2–RF during melting of $LiBH_4$ (A) and dehydrogenation (B).

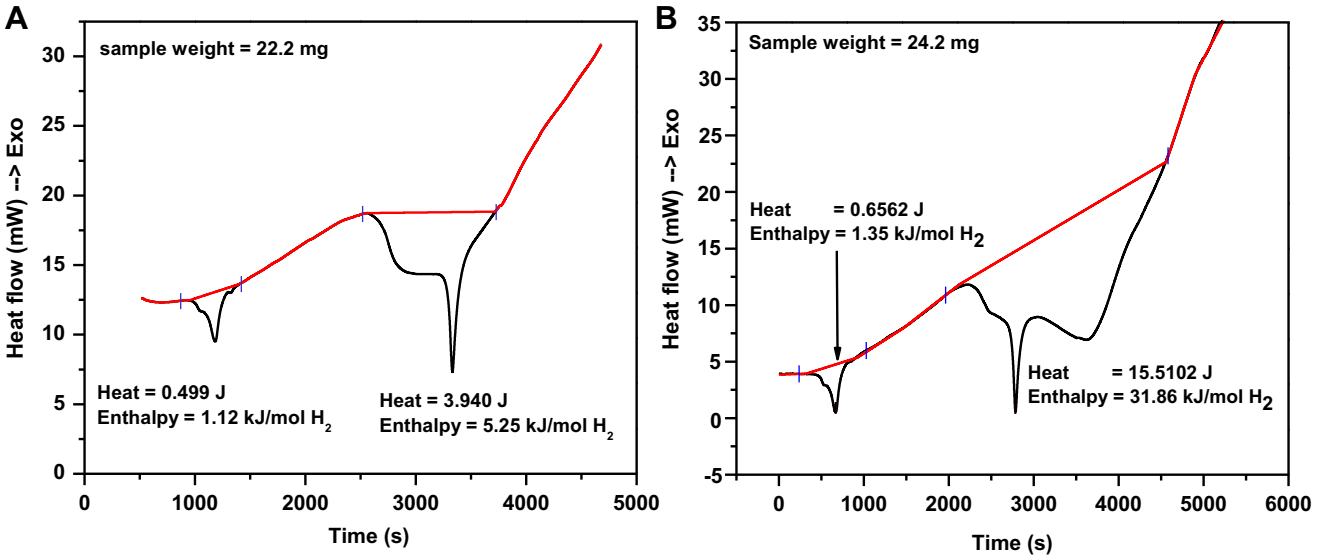

Fig. 8 – Enthalpy calculations of the nanoconfined $2LiBH_4$–$MgBu_2$–MgH_2–RF during melting of $LiBH_4$ (A) and dehydrogenation (B).

the thermodynamics was altered with nanoconfinement, thermodynamic destabilization is not found to be developed in this study. Table 2 reveals the values of $(\Delta H_{des,\ MgH_2} + \Delta H_{des,\ LiBH_4})$ for all samples and reference.

4. Conclusion

Reaction mechanisms, kinetics and thermodynamics of the recently reported nanoconfined $2LiBH_4$–MgH_2–RF and $2LiBH_4$–$MgBu_2$–MgH_2–RF samples were studied and compared with the bulk $2LiBH_4$–MgH_2. On the basis of the reaction mechanisms, both nanoconfined samples revealed mainly similar features to the bulk material; that is, the formation of MgB_2 and LiH upon dehydrogenation together with the reversibility, shown as the recovering of $LiBH_4$ and MgH_2 after rehydrogenation. Due to addition of RF–CAS for nanoconfinement of hydride composite, loss of hydrogen storage capacities was found. However, kinetic properties based on the titration results were significantly improved after nanoconfinement. Moreover, the significant reduction in activation energy as compared with the bulk material was obtained, that is, $\Delta E_A = 132$ and 27 kJ/mol for MgH_2 and $LiBH_4$ dehydrogenations, respectively, for nanoconfined $2LiBH_4$–MgH_2–RF, while those of nanoconfined $2LiBH_4$–$MgBu_2$–MgH_2–RF was 86 and 171 kJ/mol, respectively. Thermodynamic properties based on the dehydrogenation enthalpies of MgH_2 and $LiBH_4$ $(\Delta H_{des,\ MgH_2} + \Delta H_{des,\ LiBH_4})$ obtained from

both nanoconfined samples were in the range of 41.5–46.2 kJ/mol H_2, which was not significantly different from the bulk material (44.13 kJ/mol H_2).

Acknowledgment

The authors are thankful to the Institute of Science, Suranaree University of Technology, Thailand and The Alexander von Humboldt Foundation, Germany. Also, we would like to acknowledge the Research, Development and Engineering (RD&E) fund through The National Nanotechnology Center (NANOTEC), The National Science and Technology Development Agency (NSTDA), Thailand (P-11-00991) to Suranaree University of Technology. We acknowledge Dr. Jans Perlich, and Dr. Yngve Cerenius for kind help and access to the beam time at BW4 beamline (DESY, Hamburg, Germany) and I711 beamline (Max-lab, Lund, Sweden), respectively.

Appendix A. Supplementary data

Supplementary data related to this article can be found, in the online version, at http://dx.doi.org/10.1016/j.ijhydene.2012.11.064.

REFERENCES

[1] Varin RA, Czujko T, Wronski ZS. Nanomaterials for solid state hydrogen storage. New York: Springer Science + Business Media; 2009.
[2] Schlesinger HI, Brown HC. Metallo borohydrides. III. Lithium borohydride. J Am Chem Soc 1940;62(12):3429–35.
[3] Bogdanovic B, Brand RA, Marjanovic A, Schwickardi M, Tölle J. Metal–doped sodium aluminium hydrides as potential new hydrogen storage materials. J Alloys Compd 2000;302(1–2):36–58.
[4] Züttel A, Wenger P, Rentsch S, Sudan P, Mauron Ph, Emmenegger Ch. $LiBH_4$ a new hydrogen storage material. J Power Sources 2003;118(1–2):1–7.
[5] Orimo S, Nakamori Y, Kitahara G, Miwa K, Ohba N, Towata S, et al. Dehydrogenation and rehydriding reactions of $LiBH_4$. J Alloys Compd 2005;404–406:427–30.
[6] Li C, Peng P, Zhou DW, Wan L. Research progress in $LiBH_4$ for hydrogen storage: a review. Int J Hydrogen Energ 2011;36(22):14512–26.
[7] Bösenberg U, Doppiu S, Mosegaard L, Barkhordarian G, Eigen N, Borgschulte A, et al. Hydrogen sorption properties of MgH_2–$LiBH_4$ composites. Acta Materialia 2007;55(11):3951–8.
[8] Barkhordarian G, Klassen T, Dornheim M, Rüdiger B. Unexpected kinetic effect of MgB_2 in reactive hydride composites containing complex borohydrides. J Alloys Compd 2007;440(1–2):L18–21.
[9] Dornheim M, Doppiu S, Barkhordarian G, Bösenberg U, Klassen T, Gutfleisch O, et al. Hydrogen storage in magnesium–based hydrides and hydride composites. Scripta Materialia 2007;56(10):841–6.
[10] Vajo JJ, Mertens F, Ahn CC, Bowmann Jr RC, Fultz B. Altering hydrogen storage properties by hydride destabilization through alloy formation: LiH and MgH_2 destabilized with Si. J Phys Chem B 2004;108(37):13977–83.
[11] Vajo JJ, Skeith SL. Reversible storage of hydrogen in destabilized $LiBH_4$. J Phys Chem B 2005;109(9):3719–22.
[12] Liu BH, Zhang BJ, Jiang Y. Hydrogen storage performance of $LiBH_4$+1/2MgH_2 composites improved by Ce–based additives. Int J Hydrogen Energ 2011;36:5418–24.
[13] Gosalawit–Utke R, Nielsen TK, Pranzas K, Saldan I, Pistidda C, Karimi F, et al. 2$LiBH_4$–MgH_2 in a resorcinol–furfural carbon aerogel scaffold for reversible hydrogen storage. J Phys Chem C 2012;116:1526–34.
[14] Nielsen TK, Bösenberg U, Gosalawit R, Dornheim M, Cerenius Y, Besenbacher F, et al. A reversible nanoconfined chemical reaction. ACS Nano 2010;4(7):3903–8.
[15] de Jongh PE, Wagemans RWP, Eggenhuisen TM, Dauvillier BS, Radstake PB, Meeldjik JD, et al. The preparation of carbon–supported magnesium nanoparticles using melt infiltration. Chem Mater 2007;19(24):6052–7.
[16] Gross AF, Ahn CC, Van Atta SL, Liu P, Vajo JJ. Fabrication and hydrogen sorption behavior of nanoparticulate MgH_2 incorporated in a porous carbon host. Nanotechnology 2009;20:204005.
[17] Nielsen TK, Manickam K, Hirscher M, Besenbacher F, Jensen TR. Confinement of MgH_2 nanoclusters within nanoporous aerogel scaffold materials. ACS Nano 2009;3(11):3521–8.
[18] Paskevicius M, Tian HY, Sheppard DA, Webb CJ, Pitt MP, Gray EM, et al. Magnesium hydride formation within carbon aerogel. J Phys Chem C 2010;115(5):1757–66.
[19] Gross AF, Vajo JJ, Atta SLV, Olson GL. Enhanced hydrogen storage kinetics of $LiBH_4$ in nanoporous scaffolds. J Phys Chem C 2008;112(14):5651–7.
[20] Cahen S, Eymery JB, Janot R, Tarascon JM. Improvement of the $LiBH_4$ hydrogen desorption by inclusion into mesoporous carbons. J Power Sources 2009;289(2):902–8.
[21] Gosalawit–Utke R, Nielsen TK, Saldan I, Liapple D, Cerenius Y, Jensen TR, et al. Nanoconfined 2$LiBH_4$–MgH_2 prepared by direct melt infiltration into nanoporous materials. J Phys Chem C 2011;115(21):10903–10.
[22] Wagemans RWP, van Lenthe JH, de Jongh PE, Jos van Dillen A, de Jong KP. Hydrogen storage in magnesium cluster: quantum chemical study. J Am Chem Soc 2005;127(47):16675–80.
[23] Gertsman VY, Birringer B. On the room–temperature grain growth in nanocrystalline copper. Scripta Metall Mater 1994;30(5):577–81.
[24] Li WC, Lu AH, Weidenthaler C, Schüth F. Hard–templating pathway to create mesoporous magnesium oxide. Chem Mater 2004;16(26):5676–81.
[25] Halsey G. Physical adsorption on non–uniform surfaces. J Chem Phys 1948;16(10):931–8.
[26] de Boer JH, Linsen BG, Th Plas, Zondervan G. Studies on pore systems in catalysts: VII. Description of the pore dimensions of carbon blacks by the t method. J Catal 1965;4(6):649–53.
[27] Brunauer S, Emmet PH, Teller E. Adsorption of gases in multimolecular layers. J Am Chem Soc 1938;60(2):309–19.
[28] Barrett EP, Joyner LG, Halenda PP. The determination of pore volume and area distributions substances. I. Computations from nitrogen isotherms. J Am Chem Soc 1951;73(1):373–80.
[29] Pranzas PK, Dornheim M, Bösenberg U, Fernandez JRA, Goerigk G, Roth SV, et al. Small–angle investigations of magnesium hydride used as a hydrogen storage material. J Appl Crystallogr 2007;40:s383–7.
[30] Cerenius Y, Ståhl K, Svesson LA, Ursby T, Oskarsson Å, Albertsson J. The crystallography beamline I711 at MAX II. J Synchrotron Rad 2000;7:203–8.
[31] Milanese C, Garroni S, Girella A, Mulas G, Berbenni V, Bruni G, et al. Thermodynamic and kinetic investigations on pure and doped $NaBH_4$–MgH_2 system. J Phys Chem C 2011;115:3151–62.

[32] Li J, Wang X, Huang Q, Gamboa S, Sebastian PJ. Studies on preparation and performances of carbon aerogel electrodes for the application of supercapacitor. J Power Sources 2006; 158(1):784–8.
[33] Zhang J, Huang YN, Mao C, Peng P, Shao YM, Zhou DW. Ab initio calculations on energetics and electronic structures of cubic Mg_3MNi_2 (M = Al, Ti, Mn) hydrogen storage alloys. Int J Hydrogen Energ 2011;36(22):14477–83.
[34] Fan MQ, Sun LX, Zhang Y, Xu F, Zhang J, Chu HL. The catalytic effect of additive Nb_2O_5 on the reversible hydrogen storage performances of $LiBH_4$–MgH_2 composite. Int J Hydrogen Energ 2008;33(1):74–80.
[35] NIST chemistry web – book; NIST standard reference data – base number 69, http://webbook.nist.gov/chemistry/.
[36] Vajo JJ, Olsen GL. Hydrogen storage in destabilized chemical systems. Scripta Materialia 2007;56(10):829–34.